UNIVERSIDADE FEDERAL DE VIÇOSA
CENTRO DE CIÊNCIAS EXATAS E TECNOLÓGICAS
DEPARTAMENTO DE ENGENHARIA ELÉTRICA

JOSÉ OLIMPIO BOTELHO B M DE ALMEIDA

THREE-PHASE PHOTOVOLTAIC INVERTERS DURING UNBALANCED VOLTAGE SAGS: COMPARISON OF POWER CONTROL STRATEGIES AND THERMAL STRESS ANALYSIS

VIÇOSA
2016

JOSÉ OLIMPIO BOTELHO B M DE ALMEIDA

THREE-PHASE PHOTOVOLTAIC INVERTERS DURING UNBALANCED VOLTAGE SAGS: COMPARISON OF POWER CONTROL STRATEGIES AND THERMAL STRESS ANALYSIS

An undergraduate thesis submitted to the Department of Electrical Engineering at Universidade Federal de Viçosa, for the accomplishment of the course ELT 490 – Monografia e Seminário, in partial fulfillment for the Degree of Bachelor in Electrical Engineering.
Supervisor: Prof. Dr. Heverton Augusto Pereira

VIÇOSA
2016

JOSÉ OLIMPIO BOTELHO B M DE ALMEIDA

THREE-PHASE PHOTOVOLTAIC INVERTERS DURING UNBALANCED VOLTAGE SAGS: COMPARISON OF POWER CONTROL STRATEGIES AND THERMAL STRESS ANALYSIS

Monografia apresentada ao Departamento de Engenharia Elétrica do Centro de Ciências Exatas e Tecnológicas da Universidade Federal de Viçosa, para a obtenção dos créditos da disciplina ELT 490 – Monografia e Seminário e cumprimento do requisito parcial para obtenção do grau de Bacharel em Engenharia Elétrica.

Aprovada em 02 de Dezembro de 2016.

COMISSÃO EXAMINADORA

Prof. Dr. Heverton Augusto Pereira - Orientador
Universidade Federal de Viçosa

Prof. M.Sc. Allan Fagner Cupertino - Membro
Centro Federal de Educação Tecnológica de Minas Gerais

Prof. Dr. - Membro
Universidade Federal de Viçosa

Prof. Dr. - Membro
Universidade Federal de Viçosa

“The ones who are crazy enough to think
that they can change the world,
are the ones who do.”

Steve Jobs

Dedicated to my parents
for their exceptional love to the family
and
to my brothers

Acknowledgements

First, I would like to thank my parents, José Mendes de Almeida Filho and Josélia Botelho Barbosa, and my brothers, Guilherme and Gustavo for their unconditional love and continual support for me throughout my life. Furthermore, I would like to thank my girlfriend, Helen, for her encouragement and support in all areas of my life.

I would like to thank my professor Heverton Augusto Pereira and Allan Fagner Cupertino for sharing their wisdom and knowledge so diligently, and for their guidance and support when needed. The opportunity to work in GESEP has provided me with countless invaluable educational experiences and has given me greater confidence in my abilities.

Furthermore, I show my gratitude to the Universidade Federal de Viçosa for their support during these five years of study. In addition, I would like to thank the University for giving me the opportunity to study abroad at the State University of New York, where I made life-long friends and had great experiences.

Finally, I would like to thank my friends for being there when I needed them and for their support in university life. A special thank you to ELT 2011. You will always be remembered.

Abstract

Unbalanced voltage sags are common and lead to instabilities in grid-connected photovoltaic systems. Such unbalanced faults generate issues in the control of negative-sequence reference voltage. Consequently, undesirable active power oscillations appear in the system. These oscillations are reflected on the DC bus voltage control, which may lead to instabilities in the system. In order to solve this problem, four different power control strategies for unbalanced voltage conditions are analyzed in this undergraduate thesis: Instantaneous Active-Reactive Control (IARC), Positive- and Negative-Sequence Control (PNSC), Average Active-Reactive Control (AARC), and Balanced Positive-Sequence Control (BPSC). Each one of these strategies shows different features, for example, cancellation of active power oscillations, balanced and sinusoidal currents delivered to the grid, or current regulation for positive and negative sequence. Focusing on the dynamic response of the system and the thermal stress of the switches, this work provides a clear comparison between the aforementioned techniques when applied to three-phase photovoltaic systems. In terms of DC bus voltage control, IARC and PNSC present no oscillations and better response. However, the IARC's reference current present high order harmonics and PNSC shows worse thermal response.

Resumo

Afundamentos de tensão desequilibrados são problemas comuns na rede e resultam em instabilidades nos sistemas fotovoltaicos conectados à rede. Esses desequilíbrios na rede geram problemas no controle da tensão de referência de sequência negativa. Consequentemente, oscilações de potência ativa indesejáveis aparecem no sistema. Tais oscilações são diretamente refletidas no controle da tensão de barramento CC, resultando em maiores instabilidades no sistema. Para resolver esse problema, quatro estratégias de controle das oscilações de potência para sistemas fotovoltaicos sob a influência de uma rede desequilibrada são analisadas nessa monografia: Controle de Potência Ativa e Reativa Instantânea (CARI), Controle de Sequência Positiva e Negativa (CSPN), Controle Médio de Potência Ativa e Reativa (CMAR), e Controle Balanceado de Sequência Positiva (CBSP). Cada uma dessas estratégias apresenta diferentes características, como por exemplo, cancelamento das oscilações de potência ativa e reativa, injeção de correntes totalmente balanceadas na rede e regulação de corrente de sequência positiva e negativa. Tendo como foco a resposta dinâmica do sistema e o stress térmico das chaves, esse trabalho fornece uma clara comparação entre as técnicas mencionadas anteriormente quando aplicadas a sistemas fotovoltaicos trifásicos. Em relação ao controle da tensão de barramento CC, os métodos CARI e CSPN apresentaram cancelamento nas oscilações de potência ativa e consequentemente melhor resposta. Entretanto, a corrente de referência no método CARI apresenta harmônicos de ordem superior e o CSPN tem um comportamento térmico indesejado.

Content

List of Figures

List of Tables

1 Introduction

This chapter gives the background, motivation and organization of this work. Photovoltaic (PV) systems and distributed power generation systems, voltage sags, as well as some challenges for the integration of PV systems into the electrical grid are presented. Then the objectives and structure of this undergraduate thesis are outlined.

1.1 PV systems and the Distributed Power Generation Systems

Solar power generation is one of the most reliable and rapidly growing renewable energy sources. Photovoltaic (PV) cells is a common method for generating electrical power from the sunlight. PV systems were originally used in isolated and stand-alone applications. However, the tendency now is to connect these systems to the public grid, in order to obtain a more robust and resilient power grid. In the last few years, there have been an increasing number of PV generators integrated into an electrical grid. In fact, PV systems experienced another year of record growth in 2015. The annual report for new capacity, Figure 1, shows an increase of 25% in comparison to 2014. More than 50 GW were added – equivalent to an estimated 185 million solar panels – bringing total global capacity to about 227 GW. The annual market was nearly 10 times the size of cumulative world capacity just a decade earlier [1]–[3].

Distributed power generation systems (DG) have changed our conception of reliable electrical grids. The increasing growth of the power demands, along with the possibility to generate electricity in areas close to the consumers, allows the reduction of losses on long transmission lines and also support the electrical grid [4]. Hence, the DG is becoming a part of the strategic plans of most countries to address current challenges associated with energy management. The new electrical grid has to be able to deliver electricity from suppliers to consumers more efficiently, reliably and transparently [4], [5].

Most of the benefits of employing DG in existing distribution networks have both economic and technical implications and they are interrelated. While all the benefits can be valuated in terms of money, some of them have stronger technical influence than others. As such, it is proposed to classify the benefits into two groups—technical and economic [6]. The major technical benefits are:

- reduced line losses;
- reduced emissions of pollutants;

- increased overall energy efficiency;
- enhanced system reliability and security.

The major economic benefits are:

- deferred investments for upgrades of facilities;
- enhanced productivity;
- reduced fuel costs due to increased overall efficiency;
- reduced reserve requirements and the associated costs;
- increased security for critical loads.

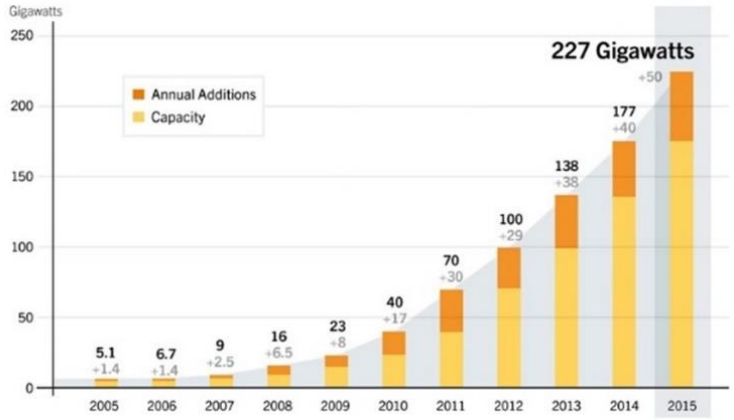

Figure 1 – Solar PV global capacity and annual additions, 2005-2015 [1]

1.2 Voltage Sags

Voltage sags are a common power quality problem. Despite being a short duration event during which a reduction in the root-mean-square (rms) voltage magnitude takes place, a small reduction in the system voltage can cause serious consequences. Voltage sag is defined as a decrease of rms voltage from 0.1 to 0.9 per unit (pu), for a duration of 0.5 cycle to 1 minute, considered the most common power quality issue. These faults are usually caused by motor starting, short circuits and fast reclosing of circuit breakers [7]–[10].

The dips (voltage sags) are among the most difficult events to be monitored, as they are caused by random and unpredictable factors. It is not only difficult to measure the magnitude and duration that characterizes them, but also in determining its frequency of occurrence, the starting time, the cause and its propagation in the system.

A voltage sag is classified as balanced or unbalanced sag, and depending on magnitude severity it is classified in shallow and deep sag as shown below in Figure 2. Depending on the nature of the fault (e.g., symmetrical or unsymmetrical), the magnitudes of voltage sags can be equal in each phase or unequal, respectively. For a fault in the transmission system, customers do not experience interruption, since transmission systems are looped/networked.

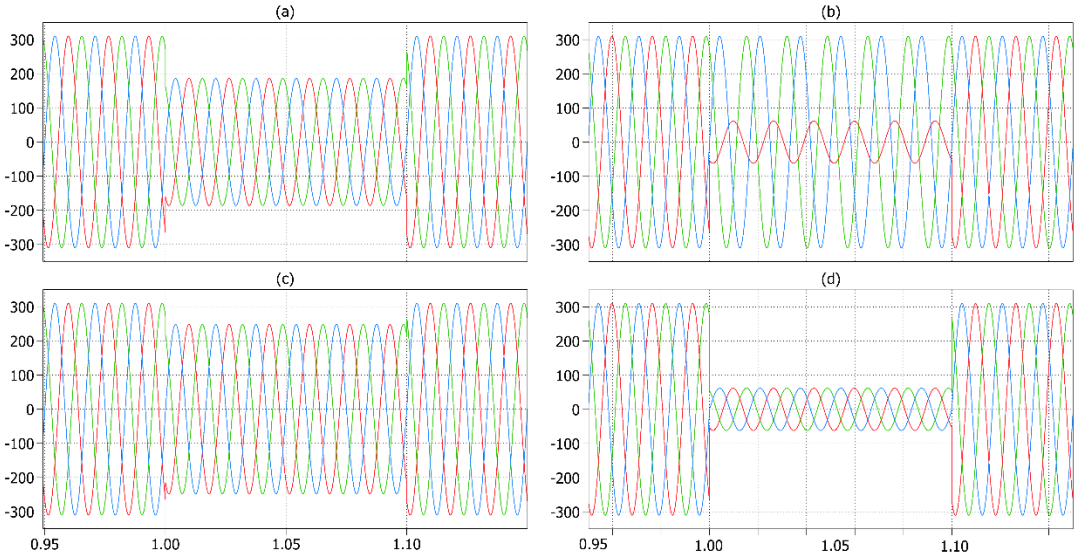

Figure 2 – (a) Balanced and (b) unbalanced voltage sag; (c) shallow and (d) deep sag.

1.3 Problem Statement

The challenge now is to propose a robust and efficient control method for the integration of PV systems to the public grid, in terms of response to grid faults. Occurrences of these faults usually give rise to the appearance of unbalanced grid voltages at the point of connection of the power converter. Under unbalanced conditions, the currents injected into the grid lose their sinusoidal and balanced appearance. However, the currents injected by the power converter into the phases of the grid should always be under control, even though the grid voltage experiences strong variations. The injection of balanced currents into the grid cannot be accurately achieved by using most of the conventional current controllers currently implemented in the industry. For this reason, some improved control structures specifically designed to inject unbalanced currents into the grid as proposed in [11], will be studied.

During a voltage sag, one or more phase voltages are reduced and the currents supplied by the PV system need to be increased to maintain the same amount of injected power as in nominal conditions. The source should be able to override the large currents caused by temporary voltage sags, and continue feeding the grid according to the standards. These

overcurrents, which can double the nominal values, can damage the power systems and switches as well as the interconnection lines [12]. Under these conditions, the currents injected to the grid lose the balanced aspect, giving rise to undesirable current transients, in addition to active and reactive power oscillations delivered to the grid. Active power oscillations implies in larger oscillations on the DC bus voltage, which may affect the system effectiveness.

Another important issue highlighted in this work is the thermal response of the converter during the voltage sags. In fact, the most frequently observed failure mechanisms are related to thermal stresses, which depends on the temperature swings and mean junction temperature of the power devices [13], [14]. In other words, the system's thermal behavior directly affects the reliability of the PV system and its lifetime.

1.4 Objectives

The main purpose of this undergraduate thesis is to explore and compare four different control strategies for the three-phase PV inverter connected to the grid during a voltage sag. These different strategies, Instantaneous Active-Reactive Control (IARC), Positive- and Negative-Sequence Control (PNSC), Average Active-Reactive Control (AARC), and Balanced Positive-Sequence Control (BPSC) are presented in [11], and will be better studied along this work. Each one of these strategies shows different features, for example, cancellation of active power oscillations, balanced and sinusoidal currents delivered to the grid, or current regulation for positive and negative sequence. The contributions of this work are focused in the comparison of these strategies in terms of thermal stress, switching/conduction losses, and the effect on the DC bus voltage during a voltage sag.

1.5 Project Outline

The structure of the thesis is organized as follows:

Chapter 1 presents the introduction and motivation of the whole thesis, where the background, objectives, and structure are addressed.

In Chapter 2, the PV inverter model and its topology are first presented and a literature review about the modelling process is shown. The solar panel model, system topology, LCL filter design, pulse-width modulation, synchronism structure and the thermal model are explored as a bibliographic review for this work.

Chapter 3 discusses the general control strategy for the system. The boost converter control is proposed, as well as proportional multi-resonant controllers used in the control. Finally, four different power oscillations control strategies are presented, highlighting different features of each.

Chapter 4 gives the study case for this work and all the simulation parameters. It also presents the voltage sag profile used on the simulations and all the results in order to make a clear comparison between the control strategies.

Finally, Chapter 5 brings the conclusions and proposes future work for this undergraduate thesis.

2 Literature Review

The background studies, necessary for modelling and simulating a photovoltaic system, are presented in this chapter. The single-diode approach for modelling the photovoltaic cell is first presented, and then the system topology, LCL filter design, switching method and synchronism structure are discussed. Finally, the thermal modelling is explored in order to achieve a more complete PV system model.

2.1 Photovoltaic Cell

A photovoltaic cell is a semiconductor diode whose p–n junction is exposed to light. Photovoltaic cells are made of several types of semiconductors using different manufacturing processes. The monocrystalline and polycrystalline silicon cells are the most common found at commercial scale now. Silicon PV cells are composed of a thin layer of bulk Si or a thin Si film connected to electric terminals. One of the sides of the Si layer is doped to form the p–n junction. Figure 3 illustrates the physical structure of a PV cell. The incidence of light on the cell generates charge carriers that originate an electric current if the cell is short-circuited [15]. Charges are generated when the energy of the incident photon is sufficient to detach the covalent electrons of the semiconductor—this phenomenon depends on the semiconductor material and on the wavelength of the incident light.

The rate of generation of electric carriers depends on the flux of incident light and the capacity of absorption of the semiconductor. The capacity of absorption depends mainly on the semiconductor bandgap, on the reflectance of the cell surface (that depends on the shape and treatment of the surface), on the intrinsic concentration of carriers of the semiconductor, on the electronic mobility, on the recombination rate, on the temperature, and on several other factors [16], [17]. The solar radiation is composed of photons of different energies. Photons with energies lower than the bandgap of the PV cell are useless and generate no voltage or electric current. Photons with energy superior to the bandgap generate electricity, but only the energy corresponding to the bandgap is used—the remainder of energy is dissipated as heat in the body of the PV cell. Semiconductors with lower bandgaps may take advantage of a larger radiation spectrum, but the generated voltages are lower [18].

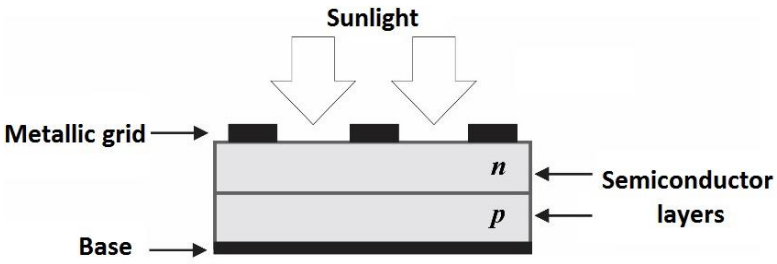

Figure 3 – Physical structure of a PV cell [18].

The study of the physics of PV cells is considerably complicated and is out of the scope of this work. For the purpose of studying electronic converters for PV systems, it is sufficient to know the electric characteristics of the PV device (cell, panel, and array). The manufacturers of PV devices always provide a set of empirical data that are used to obtain the mathematical equation of the device I–V curve. Some manufacturers also provide I–V curves obtained experimentally for different operating conditions.

2.1.1 Equivalent Model

Many literature references propose methods for modelling and simulating photovoltaic devices based on the traditional single-diode model [17]–[22]. A simplified PV panel model based on this method is shown in Figure 4.

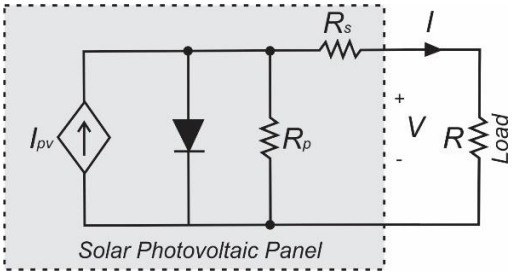

Figure 4 – Simplified photovoltaic panel model [18].

In this case, the current I through the electric terminals of a photovoltaic panel at any moment is given as

$$I = I_{pv} - I_0\left(e^{\frac{V+R_s I}{V_t a}} - 1\right) - \frac{V + R_s\, I}{R_p} \tag{1}$$

where R_S represents the electrical resistance between the cell's terminals, R_P is responsible for modelling the diode's current leakage. An algorithm for defining the values of R_P and R_S is proposed by [18]. I_{pv} is the current generated from the sunlight, I_0 is the reverse saturation current, a represent the ideal diode constant and V_t is the panel's thermal voltage and is calculated by

$$V_t = \frac{N_s k T}{q} \tag{2}$$

where N_s is the number of series-connected cells, k is the Boltzmann constant [$1,3806503 \times 10^{-23}$ J/K], T[K] is the operational temperature and q is the electron charge [$1,60217646 \times 10^{-19}$ C].

The light-generated current of the PV cell depends linearly on the solar irradiation and is also influenced by the temperature [23], [24], according to the following equation:

$$I_{pv} = \left(I_{pv_n} + K_i\, \Delta T\right) \frac{G}{G_n} \tag{3}$$

where I_{pv_n} is the light-generated current at the nominal irradiance (G_n) and temperature (T_n), usually 1000 $\mathrm{W/m^2}$ and 25 ºC, respectively. Additionally, $\Delta T = T - T_n$, G is the irradiation on the device surface, K_i is the short-circuit current temperature coefficient [A/K] [23].

The saturation current, I_0 can be evaluated as

$$I_0 = \frac{I_{sc_n} + K_i\, \Delta T}{exp\left(\frac{V_{oc_n} + K_v\, \Delta T}{a\, V_t}\right) - 1} \tag{4}$$

where I_{sc_n} is the nominal short-circuit current, V_{oc_n} is the nominal open-circuit voltage and K_v is the temperature coefficient [V/K] related to the open-circuit voltage. The practical PV device presents a hybrid behavior, which may be of current or voltage source depending on the operating point, as shown in Figure 5.

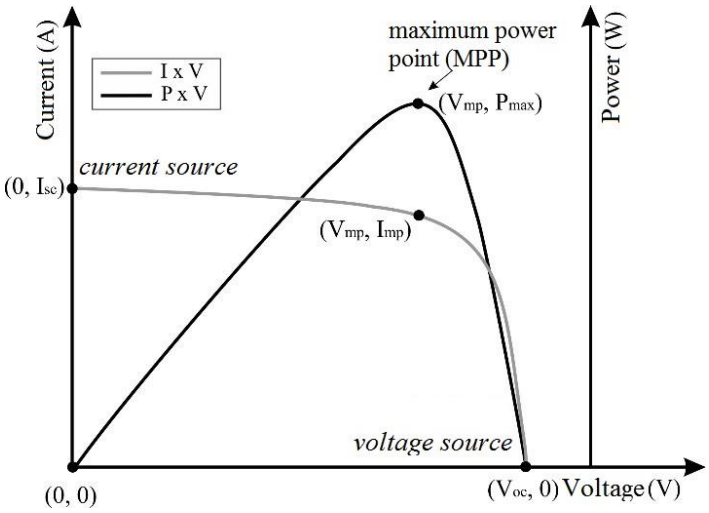

Figure 5 – IxV and PxV curves of a photovoltaic panel.

The I–V characteristic of the PV device depends on the internal characteristics of the device (R_P and R_S) and on external influences such as irradiation level and temperature. The points highlighted on the curve are: open-circuit voltage point (V_{OC}, 0), short-circuit current point (0, I_{sc}) and the maximum power point (V_{mp}, I_{mp}). Table 1 presents the model parameters of the solar panel selected for the simulations in this work.

Table 1 - Solar panel parameters used in this work.

Parameters	Value
Maximum Power	250 *W*
Maximum Power Voltage	30,5 V
Maximum Power Current	8,20 A
Open-Circuit Voltage	37,8 *V*
Short-Circuit Current	8,75 *A*
Diode constant, a	1
Coefficient K_i	0,02 *A/K*
Coefficient K_v	-0,36 *V/K*
Series Resistance R_s	0,173900 Ω
Parallel Resistance R_p	379,023365 Ω

2.2 System Topology

The main purpose of a grid-connected solar PV system is to transfer the maximum power obtained from the sun into the electric grid. This goal imposes the necessity of being constantly operating the PV system near the maximum power independently of the climatic conditions; therefore the use of an appropriate electronic interface with maximum power point tracking (MPPT) capabilities and the ability of effectively connecting to the AC power grid is required. The power conditioning system (PCS) is the electronic device that permits to achieve this objective, by successfully controlling the active power flow exchanged with grid. Even more, with the appropriate PCS topology and its control design, the PV array is capable of simultaneously and independently performing both instantaneous active and reactive power flow control, as presently required for grid connection of new distributed generation system applications. To this aim, a hardware configuration of two cascade stages is used, which offers an additional degree of freedom in the operation of the grid -connected solar PV system when

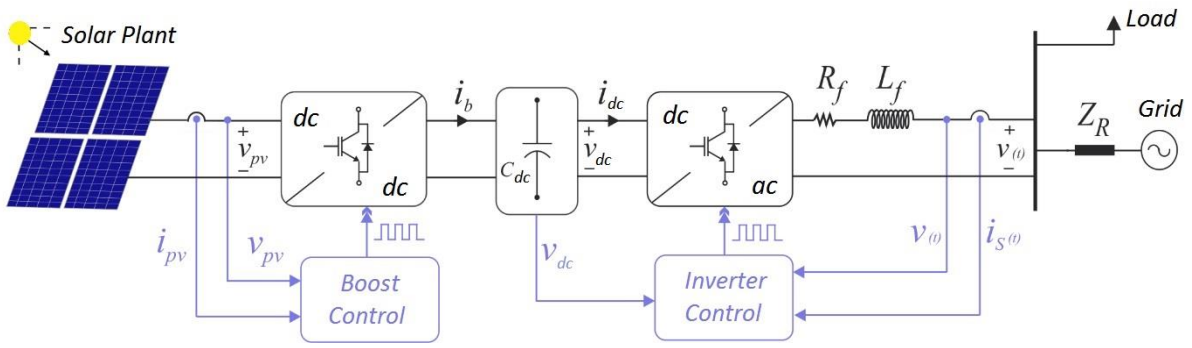

Figure 6 – Structure of PV system connected to the grid.

compared with the single-stage configuration. Hence, by including the DC/DC boost converter between the PV array and the inverter linked to the electric grid, various control objectives are possible to be pursued simultaneously and independently of the PV array operation without changing the PCS topology [25], [26].

The detailed model of the proposed grid-connected solar PV system is illustrated in Figure 6, and consists of the solar PV arrangement and its PCS to the electric utility grid. PV panels are electrically combined in series to form a string (and sometimes stacked in parallel) in order to provide the desired output power required for the application. A three-phase DC/AC voltage source inverter (VSI) using IGBTs (Insulated Gate Bipolar Transistors) is employed for connecting to the grid. This three-phase static device is shunt-connected to the distribution network in the so-called point of common coupling (PCC) by means of a coupling transformer and the corresponding line sinusoidal filter. The output voltage control of this VSI can be efficiently performed using pulse width modulation (PWM) techniques.

2.3 LCL Filter

The LCL filter is made up of three reactors with resistance R and inductance L on the converter side, three reactors with resistance R_f and inductance L_f on the grid side, and three capacitors C_f (each of them damped with a resistor R_d). A LCL filter is used to reduce high order harmonics generated by IGBT's switching, decrease switching ripple, increase stability and rapid dynamic response, and guarantee minimum requirements when injecting current into the grid. Its topology is shown in Figure 7. The detailed modelling process, as well as the parameters design can be found in [27].

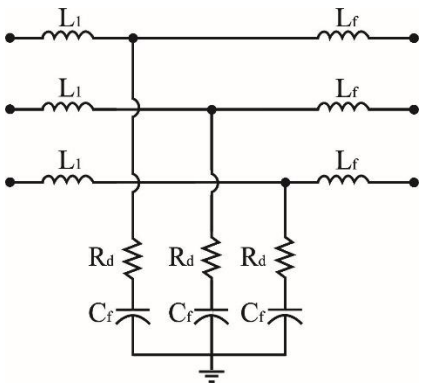

Figure 7 – LCL Filter structure.

2.4 Space Vector PWM (SVPWM)

Different modulation schemes exist for modulating DC-AC multilevel inverters [28]. The SVPWM method depends on calculating dwell times and selecting switching states and sequences. Therefore, it provides flexibility in generating gate signals. It is used to enable a better performance for multilevel inverters. Different control objectives are achieved with proper design of SVPWM such as neutral point voltage control, common-mode voltage reduction, power loss reduction, and fault tolerant control [29]–[31].

The SVPWM converts the three voltage control references in the complex αβ plane in order to generate a vector reference by selecting a proper sequence of active vectors. Redundant vectors have opposite effects on the DC bus capacitor voltage, although they generate the same output line-to-line voltage. Therefore, alternate use of these switching states is desirable for DC bus capacitor voltage balancing control. Effective utilization of redundant switching states eliminates the need of extra hardware for the capacitor voltage balancing, without affecting the dwell timing of space vector over switching period. A possible choice for implementing SVPWM is to select the nearest three vectors (NTV) to perform modulation. A detailed switching method for the three-leg inverter is shown in [32]. The mentioned inverter can generate sinusoidal output currents with independently control of magnitudes while the phase angle between them is set to 90 degrees, regardless of unequal output magnitudes.

2.5 Phase Locked Loop (PLL)

A basic PLL structure is presented as Figure 8, which consists of a Phase Detector (PD), a Proportional Integral (PI) based Loop Filter (LF) and a Voltage-Controlled Oscillator (VCO). Thus, the small signal model of this system can be obtained as

$$\frac{\hat{\Theta}(s)}{\Theta(s)} = \frac{k_p s + k_i}{s^2 + k_p s + k_i} \tag{5}$$

where $\hat{\Theta}(s)$, $\Theta(s)$ are the output and input phase respectively, and k_p, k_i are the proportional and integral gains of the loop filter. A review on PLL structures can be found in [33] . The synchronous reference frame PLL (SRF-PLL) is a standard PLL in three-phase applications and the building block of almost all advanced PLLs. This structure will be explored next.

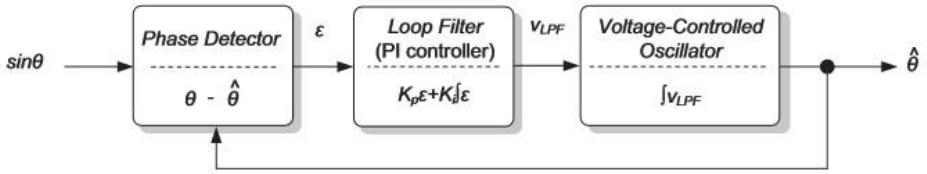

Figure 8 – Basic structure of a phase locked loop.

2.5.1 Analysis of Conventional SRF-PLL

Let the three-phase input signals of the conventional SRFPLL be as

$$\begin{aligned} v_a &= V\cos(\theta) \\ v_b &= V\cos\left(\theta - \frac{2\pi}{3}\right) \\ v_c &= V\cos\left(\theta + \frac{2\pi}{3}\right) \end{aligned} \tag{6}$$

where V and θ are the amplitude and phase angle of the three-phase signals, respectively.

Considering the Clarke's and Park's transformations as

$$T_{abc\to\alpha\beta} = \frac{2}{3}\begin{bmatrix} 1 & -\frac{1}{2} & -\frac{1}{2} \\ 0 & \frac{\sqrt{3}}{2} & -\frac{\sqrt{3}}{2} \end{bmatrix} \tag{7}$$

$$T_{\alpha\beta\to dq} = \frac{2}{3}\begin{bmatrix} \cos\hat{\theta} & \sin\hat{\theta} \\ -\sin\hat{\theta} & \cos\hat{\theta} \end{bmatrix} \tag{8}$$

and applying them to equation (6) gives:

$$v_d = V\cos\left(\theta - \hat{\theta}\right) \tag{9}$$

$$v_q = V\sin\left(\theta - \hat{\theta}\right) \tag{10}$$

where

$$\theta = \int \omega_g dt = \int (\omega_n + \Delta\omega_g) dt = \int \omega_n dt + \int \Delta\omega_g dt$$
$$\hat{\theta} = \int \hat{\omega}_g dt = \int (\omega_n + \Delta\hat{\omega}_g) dt = \int \omega_n dt + \int \Delta\hat{\omega}_g dt \quad (11)$$

Substituting equation (11), into (9) and (10) yields

$$v_d = V\cos(\Delta\theta - \Delta\hat{\theta}) \approx V$$
$$v_q = V\sin(\Delta\theta - \Delta\hat{\theta}) \approx V(\Delta\theta - \Delta\hat{\theta}) \quad (12)$$

As can be seen, the signal v_q contains the phase error information, and signal v_d is a measure of the amplitude of the three-phase signals. Using equations (11) and (12), the nonlinear and linear models of the SRF-PLL can be simply obtained as shown in Figure 9. These models provide very useful information about characteristics of the SRF-PLL.

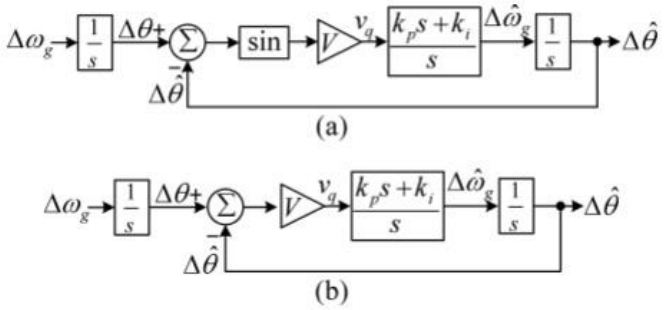

Figure 9 – (a) Nonlinear model and (b) linear model of the conventional SRFPLL.

Note, V_d = V and $V_q = 0$ when $\Delta\hat{\theta} = \Delta\theta$. Analyzing the structure in Figure 9(a) we conclude that

$$\Delta\hat{\omega}_g = \frac{d\theta}{dt} = G(s)V_q \quad (13)$$

where $G(s)$ is the transfer function of the proportional-integral (PI) controller, which can be described as:

$$G(s) = \frac{k_{p\_pll}s + k_{i\_pll}}{s} \quad (14)$$

The linear model showed in Figure 9(b) gives us the following transfer function:

$$H(s) = \frac{2\xi\omega_m s + \omega_m^2}{s^2 + 2\xi\omega_m s + \omega_m^2} \quad (15)$$

where

$$\omega_m = \sqrt{\frac{k_{p\_pll}\, V}{\tau_i}}\ e\ \xi = \frac{k_{p\_pll} V}{2\omega_m} = \frac{\sqrt{k_{p\_pll}\, \tau_i V}}{2} \tag{16}$$

Equation (16) allows the calculation of the controller gains. Usually it is acceptable $\xi = 1/\sqrt{2}$. Greater is the value of ω_m, greater it will be the PLL bandwidth and consequently faster the synchronization will take place, however, the structure will be more sensitive to grid disturbances.

2.5 Thermal Models of Power Devices and Capacitor

Power losses on the power electronics devices are inevitable, which will heat the devices. Temperature changes of the power devices will affect the reliability, as the temperature fluctuation has been one of the most observed factors that cause failures of power devices (e.g. IGBTs) [14], [34], [35]. It has been reported that the power electronics devices and the capacitors are two of the most life limiting components in a PV system [34]. In order to develop reliability-oriented control strategies and thus achieve a reduced cost of energy during lifetime, more efforts should be devoted to the thermal modelling of power devices and capacitors.

Ideally, all the solar PV energy should be transferred to the power grid. However, there are power losses e.g. on the passive components and the power devices. The power losses, which mainly include switching losses and conduction losses, of the power devices will cause temperature rise at certain points (e.g. the junction inside the device) due to the thermal impedances. In other words ,the electrical performance (electrical model) of a power device, and thus a PV inverter, is coupled with its thermal behavior (thermal model) through the power losses, as shown in Figure 10. Then, the instantaneous temperature of the power device can be expressed as,

$$\begin{aligned} T_{j(S/D)}(t) &= P_{tot(S/D)}(t) Z_{th(S/D)(j-c)}(t) + T_c(t) \\ T_c(t) &= [P_{totS}(t) + P_{totD}(t)].\left[Z_{th(c-h)}(t) + Z_{th(h-a)}(t)\right] + T_a(t) \end{aligned} \tag{17}$$

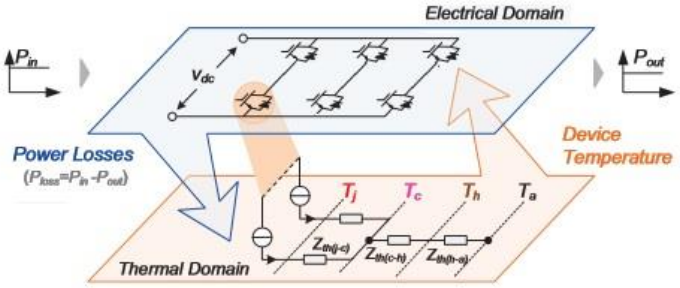

Figure 10 – Thermal model of a power device in a PV inverter.

in which, $T_{j(S/D)}$ is the IGBT/diode junction temperature, $P_{tot(S/D)}$ is the IGBT/diode total power losses, $Z_{th(S/D)(j-c)}$ is the thermal impedance from junction to case, $Z_{th(c-h)}$ is the thermal impedance from case to heat-sink, $Z_{th(h-a)}$ is the thermal impedance from heat-sink to ambient, T_c is the case temperature, T_a is the ambient temperature, and S represents the IGBT and D denotes the diode. Equation (17) shows that the ambient temperature will also influence the junction temperature. The PV power converters even with low power losses may have high junction temperatures when operating in a harsh environment.

In respect to the thermal impedance from junction to case ($Z_{th(S/D)(j-c)}$), it can be modelled as a Cauer RC network [36], which is a physical-material-based and realistic representation of the impedance, and thus it can reflect the thermal transient behavior of an IGBT module more accurately. However, the Cauer model requires an in depth material level knowledge. Thus, it is normally converted into a Foster model, of which the thermal parameters can be found in the data-sheets of the power devices. As it is shown in Figure 11, the analytical function of the thermal impedance can be described as [37], [38],

$$Z_{th(S/D)(j-c)}(t) = \sum_{i=1,2,3,4}^{n} R_{thi}(1 - e^{-t/\tau_i}) \tag{18}$$

According to equations (17) and (18), it is illustrated that the steady-state mean value ($t \to \infty$) of the junction temperature is dependent on the thermal resistance R_{thi}; while the dynamic behavior of the junction temperature is affected mainly by the thermal capacitance C_i (time constant $\tau_i = C_i R_{thi}$). Moreover, the case temperature (T_c) has a much slower dynamic response than that of junction temperature (T_j) due to much larger time-constants of the thermal impedances ($Z_{th(c-h)}$ and $Z_{th(h-a)}$) [38]. The thermal parameters for the IGBT modules used in this project are listed in Table 2.

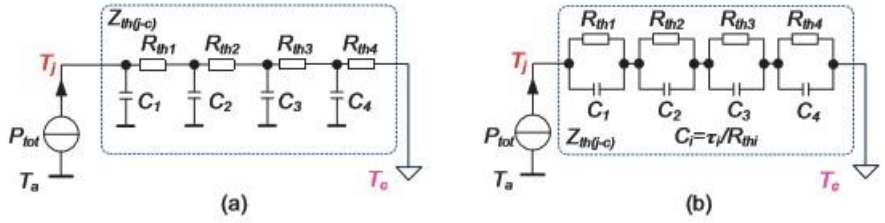

Figure 11 – Thermal impedance models: (a) Cauer model and (b) Foster model.

Table 2 - The thermal parameters of the Infineon FS35R12KT3 IGBT module.

Parameter	$Z_{th(j-c)}$					$Z_{th(c-h)}$
IGBT	R_i (K/kW)	0.06769	0.2709	0.1523	0.1052	0.02
	T_i (s)	0.00234	0.0282	0.113	0.282	
Diode	R_i (K/kW)	0.09674	0.6249	0.18	0.057	
	T_i (s)	0.00333	0.0343	0.1294	0.7662	

Similarly, due to the power losses on the Equivalent Series Resistor (ESR) of the capacitors in a PV system, failures may occur when the hot-spot temperature of the capacitor goes beyond the limitation during operations. Unlike the multi-layer model of power devices, the thermal model of capacitors is basically simple. Normally, only the thermal resistance, R_{th}, is considered, and it can be found in the data-sheets. In respect to capacitor sizing, it is determined by the following constraints:

$$\Delta V_c \approx \frac{P_0}{2\pi f_0 C V_c}, \qquad i_{c,RMS} = \frac{P_0}{\sqrt{2} V_c} \tag{19}$$

where P_0 is the average power supplied to the grid, f_0 is the fundamental frequency of the grid, ΔV_c is the peak-to-peak ripple of the decoupling capacitor voltage V_c, C is the capacitance of the capacitor, and $i_{c,RMS}$ is the RMS current flowing through the capacitor. It should be pointed out that equation (19) is not applicable to the filter capacitor (e.g. the capacitor in an LCL filter) design, where for example the reactive power absorption and resonant frequency have to be taken into account [27].

3 Multifunctional Three-Phase Photovoltaic Inverter

This chapter presents the control strategy for three-phase photovoltaic systems under unbalanced voltage grid. The basic αβ control strategy and P&O MPPT algorithm are first presented. Then, the boost converter control and the concept of Proportional Multi-Resonant (PMR) controller are introduced. Finally, the instantaneous power theory is studied in order to design specific strategies for controlling power oscillations during a voltage sag.

3.1 Control Strategy

The system's control strategy used in this work is shown in Figure 12. Disregarding to the capacitor effect on the LCL filter, the inverter response in αβ is given as

$$v_\alpha - Ri_\alpha - L\frac{di_\alpha}{dt} - V_\alpha = 0 \tag{20}$$

$$v_\beta - Ri_\beta - L\frac{di_\beta}{dt} - V_\beta = 0 \tag{21}$$

where L and R are the sum of the inductances L_1 and L_f, and the sum of the resistances R_1 and R_f respectively. ω_n is the grid frequency.

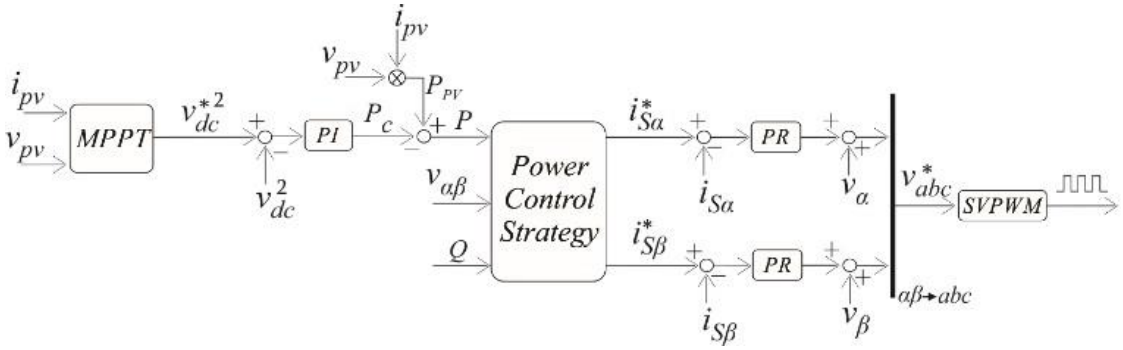

Figure 12 – Inverter control strategy.

The squared reference DC-bus voltage (v_{pv}^{*2}) used in the outer control loop, is generated by a maximum power point tracker (MPPT). Several of these algorithms have been proposed before, such as: Perturbation and Observation (P&O)[39], dP-P&O [40] e Modified P&O (MP&O) [41]. Due to its low complexity and computational requirements, the P&O method is the most common amongst PV for distributed generation applications. This algorithm tracks by

measuring the output voltage and current, calculating the power, stepping the operating voltage in a particular direction and then re-measuring and re-calculating the voltage, current and power. If the new measurement is greater (less) than the previous one then the maximum power point (MPP) is achieved if the voltage is stepped in the same (opposite) direction. After several iterations of the algorithm the MPP will be reached [39], [42]. The flow chart for P&O is shown in Figure 13.

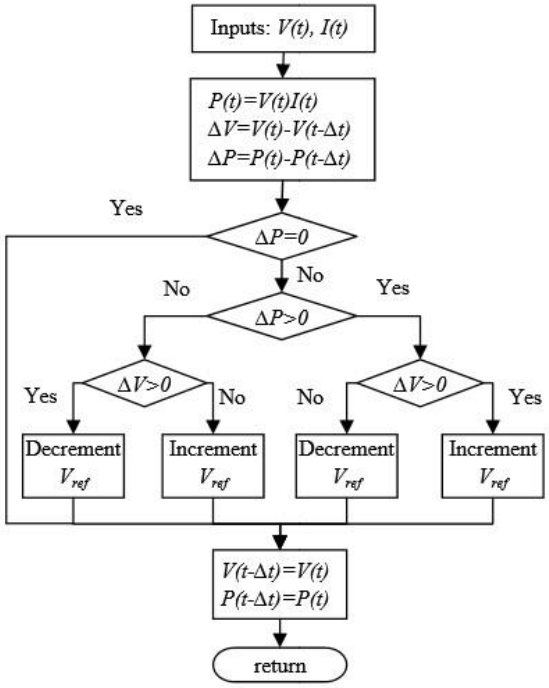

Figure 13 – Flow chart for P&O algorithm [42].

The behavior of the dc-bus capacitor can be represented by the energy storage (W) stored in its terminals, i.e.

$$W = \frac{1}{2} C_{dc} v_{pv}^2 \tag{22}$$

The time derivative of the W represents the instantaneous power stored in the capacitor p_{cap}. As follows, the injected power by the inverter (p_{inv}) is given by

$$p_{inv} = p_{pv} + p_{cap} \tag{23}$$

Thus, the relation between p_{cap} and v_{pv} is expressed by

$$v_{pv}^2 = \frac{p_{cap}}{2C_{dc}s} \tag{24}$$

Thereby, considering the ideal inner loop, the outer closed-loop (G_{out}) is obtained as:

$$G_{out} = \frac{v_{pv}^2}{v_{pv}^{*2}} = \frac{2k_p(\tau_i s + 2)}{\tau_i C_{dc} s^2 + 2k_p(\tau_i s + 2)} \quad (25)$$

where k_p and τ_i are the PI controller parameters. The poles allocation method is used to tune the PI controller, ensuring a desired response of the DC-bus voltage.

Finally, proportional resonant controller is used to control the sinusoidal currents in stationary coordinates. It simplifies the control system, since it makes possible to control the current components of negative-sequence with no need to increase the control structure. PMR controller will be better explained in section 3.3.

3.2 Boost Control

DC-DC converters can be used as switching mode regulators to convert an unregulated dc voltage to a regulated dc output voltage. For better understanding of the connection between the boost converter and the PV plant, it is required the linear model of the PV panel. The linearization of the PV model is fulfilled, preferably, around the maximum power point (V, I), due to the fact that, many hours during the day, the system operates around this point. In [43], the author describes with details the method for linearization used in this work, and only some important points will be addressed in this chapter.

The linear model of the PV panel in a single-point is represented in equation (26). This equation was introduced in chapter 2 during the PV panel modelling, however, to standardize the variable names in this chapter, the variables I and V in the original equation are replaced for the variables i_{pv} and v_{pv}.

$$i_{pv} = I_{pv} - I_0\left(e^{\frac{v_{pv}+R_s i_{pv}}{V_t a}} - 1\right) - \frac{v_{pv} + R_s\, i_{pv}}{R_p} \quad (261)$$

Figure 14(a) shows the $i_{pv} \times v_{pv}$ curve and its linearization on the maximum power point, which can represented by the equivalent circuit shown in Figure 14(b), R_{eq} is given as:

$$R_{eq} = -\frac{1}{m}\frac{N_s}{N_p} \quad (27)$$

where m is the angular coefficient of the tangent line on the point of interest, N_s is the number of PV panels series-connected and N_P is the number of parallel-connected panels.

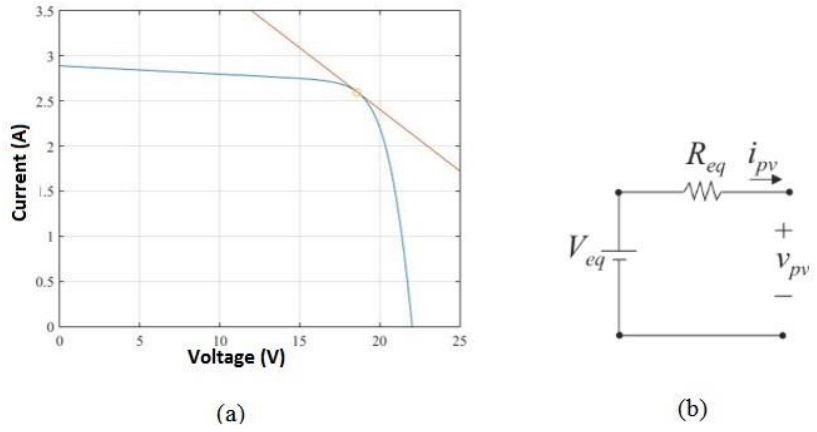

Figure 14 – (a) PV panel curve and (b) equivalent circuit on the maximum power point.

It is important to highlight that the connection between the boost converter and the modules depends on the chosen point for the linearization [43]. Conventionally, the system is projected to operate on the maximum nominal power and lately other operational points can be analyzed and made appropriate.

Thereafter the linearization of the solar panel, the small-signals model of the boost converter connected to the PV modules is shown in Figure 15. This model aims to describe the behavior of the input voltage v_{pv} in the converter, related to the control variable of the outer loop, which is the induction current i_L in *boost*. On the other hand, this current is described by the inner loop control variable, the duty cycle d of the converter. In this way, it is possible to calculate the correct controller gains for inner and outer loops. For this process, the boost converter output is represented as a DC voltage source v_{cc}, $\bar{v}$ is the mean value of v, V represents its stationary value and the small disturbs are called $\tilde{v}$.

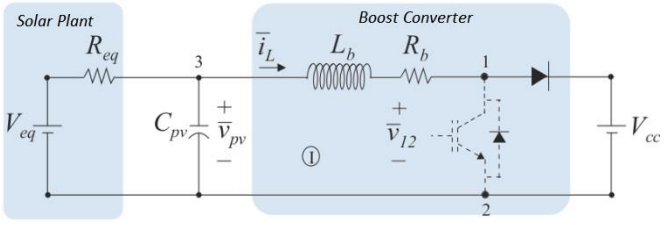

Figure 15 – DC/DC boost converter model.

The equation that represents the currents on the node 3 is given as:

$$\frac{V_{eq} - \bar{v}_{pv}}{R_{eq}} - C_{pv}\frac{d\bar{v}_{pv}}{dt} - \bar{\imath}_L = 0 \tag{282}$$

When the transistor is ON, $\bar{v}_{12} = 0$, otherwise $\bar{v}_{12}$ is equal to the converter output V_{cc}. Which leads to the following,

$$\bar{v}_{12} = (1 - d)V_{cc} \tag{29}$$

The small-signals variables in this model are presented in equation (30).

$$\bar{v}_{pv} = V_{pv} + \tilde{v}_{pv} \;\; ; \;\; \bar{\imath}_L = I_L + \tilde{\imath}_L \;\; ; \;\; d = D + \tilde{d} \tag{303}$$

Applying the definitions from equation (30) in (28), leads to the following expression:

$$\frac{V_{eq}}{R_{eq}} - \frac{V_{pv}}{R_{eq}} - \frac{\tilde{v}_{pv}}{R_{eq}} - C_{pv}\frac{d\tilde{v}_{pv}}{dt} - I_L - \tilde{\imath}_L = 0 \tag{31}$$

Finally, after the Laplace transform in equation (31) and evaluating only the small-signals, it is obtained the equation (32):

$$-\frac{\tilde{v}_{pv}(s)}{R_{eq}} - C_{pv}s\tilde{v}_{pv}(s) - \tilde{\imath}_L(s) = 0 \tag{32}$$

Through this equation is possible to estimate the transfer functions of the boost converter used in this work. $G_{vi}(s)$ relates the output $\tilde{v}_{pv}$ with the control variable $\tilde{\imath}_L$, is given as:

$$G_{vi}(s) = \frac{\tilde{v}_{pv}(s)}{\tilde{\imath}_L(s)} = -\frac{1}{C_{pv}s + \frac{1}{R_{eq}}} \tag{33}$$

Considering the capacitor voltage as input of the boost converter controlled by V_{pv}, the equation of the mean voltage values on loop I can be written as:

$$V_{pv} - L_b\frac{d\bar{\imath}_L}{dt} - \bar{\imath}_L R_b - \bar{v}_{12} = 0 \tag{34}$$

Replacing (29) in (34) and applying the definitions from equation (30), results in:

$$V_{pv} - L_b\frac{d\tilde{\imath}_L}{dt} - I_L R_b - \tilde{\imath}_L R_b - V_{cc} + V_{cc}D + V_{cc}\tilde{d} = 0 \tag{35}$$

Again, after a Laplace transform and evaluating only the small-signals, obtain:

$$-L_b s\tilde{\imath}_L(s) - \tilde{\imath}_L(s)R_b + V_{cc}\tilde{d}(s) = 0 \tag{36}$$

From equation (36), it is obtained the second transfer function of the system, $G_{id}(s)$, that relates the inductor current with the duty cycle of the converter. This transfer function can be represented as:

$$G_{id}(s) = \frac{\tilde{\imath}_L(s)}{\tilde{d}(s)} = \frac{V_{cc}}{L_b s + R_b} \tag{37}$$

Considering the PI controller's transfer function of the inductor current control loop as $K_{p_i} + K_{i_i}/s$. The gains adjust are accomplished by pole allocation methods, in order to cancel one of the system poles. This results in the following gains:

$$\begin{cases} K_{p_i} = \dfrac{2\pi f_{ci} L_b}{V_{cc}} \\ K_{i_i} = \dfrac{2\pi f_{ci} R_b}{V_{cc}} \end{cases} \tag{38}$$

where f_{ci} is the cut-off loop frequency. Its value is usually limited as one decade lower than the switching frequency of the converter, f_{sb}. This is necessary to despise the delays generated from the converter and sensor, for example.

Similarly, considering the PI controller's transfer function of the capacitor voltage control loop as $(K_{p_v} + K_{i_v})$, and the transfer function $G_{vi}(s)$ with the same pole allocation method as shown in equation (38). It results in the following controller gains for the capacitor voltage control:

$$\begin{cases} K_{p_v} = -2\pi f_{cv} C_{pv} \\ K_{i_v} = \dfrac{-2\pi f_{cv}}{R_{eq}} \end{cases} \tag{39}$$

where f_{cv} is the cut-off frequency of the voltage loop. This frequency is set as five times lower than the cut-off frequency of the current loop in order to secure the cascade operation between the systems.

3.3 Proportional Multi-Resonant Controller

The linear controllers are the most used among power conversion systems due to its high performance in tracking the signals, even when the signal has several frequencies. The conventional proportional-integral (PI) compensators falls into this category. Due to the infinite gain in the zero frequency, the application of this controller in the current control of the PV system is recommended when the inverter current reference is constant, i.e. when the inverter current control is based on synchronous reference frame. However, when it is used αβ or abc control strategy or inserted the harmonic current compensation capability in the inverter control, other linear controller has been widely used in the literature, the proportional multi-resonant (PMR) controller [44]–[46].

The PMR controller is composed of a proportional controller and can have several resonant controllers tuned at each frequency present in the signal. The PMR transfer function is given by:

$$G_{PR}(s) = K_P^{PR} + \overbrace{\sum_{h=1}^{n} K_{ih}^{PR} \frac{s}{s^2 + \omega_h}}^{R_h(s)} \tag{40}$$

where $K_P^{PR}$is the proportional gain, h is the harmonic order (h = 1,2,3...,n), ω_h are resonant frequencies and K_{ih}^{PR} are the integral gains for each harmonic frequency. It is not recommended to tune the PMR controller through phase margin and crossover frequency analysis, as it is done with PI controllers. In this way, the PMR tuning through critical point analysis in Nyquist diagram is addressed in [45].

The PMR controller has high gains at its resonant frequencies. Thereby, the terms $R_h(s)$ are responsible for tracking the current components at ω_h frequencies. The discretization method recommended for $R_h(s)$ is the Tustin with prewarping. This technique avoids the shift of the resonant frequency for which it was tuned, in this way the $R_h(z)$ is given by [47]:

$$G_{PR}(z) = \frac{sin(\omega_h T_s)}{2\omega_h} \frac{1 - z^{-2}}{1 - 2z^{-1}\, cos(\omega_h T_s) + z^{-2}} \tag{41}$$

The parameters are adjusted in accordance with reference [45], which considers the crossover frequency of the controller and its relationship with the critical point on Nyquist diagram.

3.4 Instantaneous Power Theory (IPT)

The instantaneous power theory, or p−q theory, defines a set of instantaneous powers in the time domain. Since this theory does not impose any restriction to waveforms, it is applicable to nonsinusoidal currents and voltages and not only on steady state but also during transient states [48]. IPT is widely used to detect the disturbances presents in the load current for compensation. This method also consists to separate the load current signal in three orthogonal components: active, reactive and oscillation components. Description details about this theory are shown in [49], [50].

When IPT was proposed, the main application was for active power filters. In this case, the three phase voltage and load current are measured and transformed for stationary coordinates (αβ0). From these currents and using equation (42), the zero sequence power p_0, real power p and reactive power q are calculated, where p_0 is zero if the three phase system is balanced. Currents and voltages in (42) may contain unbalances and harmonic components. Thus, in more general case p_0, p and q will have mean and oscillating components, as represented in equation (43), where the term "$\bar{p}$" represents mean value and the term "$\tilde{p}$" oscillating value.

$$\begin{bmatrix} p_0 \\ p \\ q \end{bmatrix} = \begin{bmatrix} v_0 & 0 & 0 \\ 0 & v_\alpha & v_\beta \\ 0 & v_\beta & -v_\alpha \end{bmatrix} \begin{bmatrix} i_0 \\ i_\alpha \\ i_\beta \end{bmatrix} \tag{42}$$

$$\begin{aligned} p &= \bar{p} + \tilde{p} \\ q &= \bar{q} + \tilde{q} \end{aligned} \tag{43}$$

Using a high pass filter, the oscillating components $\tilde{p}$ and $\tilde{q}$ are separated from $\bar{p}$ and $\bar{q}$. Therefore, considering a balanced system, the oscillating currents $\tilde{\imath}_\alpha$ and $\tilde{\imath}_\beta$ can be calculated by:

$$\begin{bmatrix} \tilde{\imath}_\alpha \\ \tilde{\imath}_\beta \end{bmatrix} = \frac{1}{{v_\alpha}^2 + {v_\beta}^2} \begin{bmatrix} v_\alpha & v_\beta \\ v_\beta & -v_\alpha \end{bmatrix} \begin{bmatrix} \tilde{p} \\ \tilde{q} \end{bmatrix} \tag{44}$$

It is observed that the reactive power corresponds to the parts of instantaneous power that is dependent on the instantaneous imaginary power q. On the other hand, instantaneous real power p, gives the grid energy per second being transported from source to load and vice-versa at any time, which is dependent only on the voltage and currents in phases α and β and has no zero-sequence present.

3.5 Power Control under Unbalanced Grid Conditions

The control of the instantaneous active and reactive power exchanged with the grid, and mainly the power oscillating terms that appear due to the interaction between voltages and currents with different sequences, requires the design of specific strategies for calculating the current that should be injected into the grid by the power converter. However, implementation of these strategies gives rise to the injection of unbalanced currents into the network. Therefore, specific current control structures, able to properly regulate the positive- and negative-sequence components, are necessary in order to obtain satisfactory results.

In the forthcoming study, the different techniques for calculating reference currents will be developed using a generic vector approach. This kind of analysis permits a generalized study to be carried out that is valid in either a stationary or a synchronous reference frame. Before conducting further developments, some assumptions, which will be considered from this point on, should be introduced [11]:

- The energy source supplying power through the inverter exhibits slow dynamics and hence the energy yield can be assumed as a constant throughout a grid period.
- The reference for the instantaneous active and reactive powers to be supplied by the grid connected converter canal so be considered constant throughout each grid cycle,i.e. $p^* = P$ and $q^* = Q$.
- The distributed power generator delivers power into the electrical network through a three phase three-wire connection; hence there is no active power contribution from zero-sequence current components. Thus, the zero-sequence voltage component of the grid voltage will be neglected.
- The positive- and negative-sequence components of the grid voltage have been accurately estimated using a precise grid synchronization system.

Considering these assumptions, and according to the instantaneous power theory [49], the instantaneous active power, p, supplied or drained by a grid-connected three-phase power converter can be calculated as

$$p = \boldsymbol{v}.\boldsymbol{i} \tag{45}$$

where $\boldsymbol{v} = (v_a, v_b, v_c)$ is the voltage vector in the point of common coupling (PCC), $\boldsymbol{i} = (i_a, i_b, i_c)$ is the injected current vector in such a point and '.' represents the dot product of both vectors. Considering the symmetrical components of the voltage and the current, the previous expression can be rewritten as

$$p = (v^+ + v^-).(i^+ + i^-) \tag{46}$$

$$p = \underbrace{v^+.i^+ + v^-.i^-}_{P} + \underbrace{v^+.i^- + v^-.i^+}_{\tilde{p}} = P + \tilde{p} \tag{47}$$

where v^+, v^-, i^+ and i^- are the positive- and negative-sequence vector components of the voltage and the current vectors while P and $\tilde{p}$ are the average value and the oscillatory term of the active power respectively.

On the other hand, the instantaneous reactive power q generated by the power converter, due to the interaction between the current vector i and the generic voltage vector v, can be written as

$$q = |v \times i| \tag{48}$$

Hence, the instantaneous reactive power can be defined as the module of the cross-product between v and i. However, the instantaneous reactive power can also be calculated by means of the following dot product:

$$q = \boldsymbol{v}_\perp.\boldsymbol{i} \tag{49}$$

where $\boldsymbol{v}_\perp$ is an orthogonal version (90◦ leaded) of the original grid voltage vector $\boldsymbol{v}$. The reactive power shown in equation (49) can be written as well as a function of the voltage and the current symmetrical components, giving rise to

$$q = (\boldsymbol{v}_\perp{}^+ + \boldsymbol{v}_\perp{}^-).(i^+ + i^-) \tag{50}$$

$$q = \underbrace{\boldsymbol{v}_\perp{}^+.i^+ + \boldsymbol{v}_\perp{}^-.i^-}_{Q} + \underbrace{\boldsymbol{v}_\perp{}^+.i^- + \boldsymbol{v}_\perp{}^-.i^+}_{\tilde{q}} = Q + \tilde{q} \tag{51}$$

It is shown that the reactive power can also be split into a constant component, Q, and an oscillatory term $\tilde{q}$.

In the following sections, four different strategies for determining the reference current vector, i^*, to deliver given active and reactive power set-points, P and Q, under unbalanced grid

voltage conditions, are presented as proposed in [11]. The detailed calculation of these reference currents are found in the same reference. The performance of these strategies for calculating reference currents will be compared and discussed, stressing the advantages and drawbacks of each one from the grid integration and the current injection control points of view. In these strategies, it has been assumed that no reactive power should be injected to the grid ($q^* = 0$).

3.5.1 Instantaneous Active–Reactive Control (IARC)

According to equations (45) and (48), and according to that stated in the previous chapter about instantaneous power theory, any current vector aligned with the voltage vector v will give rise to active power, while any current vector aligned with $\boldsymbol{v}_\perp$ generates reactive power. Then,

$$i_p^* = g\, v \tag{52}$$

$$i_q^* = b\, v_\perp \tag{53}$$

The current references i_p^* and i_q^* can be considered as active and reactive currents vectors respectively, representing g an instantaneous conductance and b an instantaneous susceptance, both real terms, which sets the proportion between the voltage and the current vectors. The value of these terms that give rise to the exchange of a certain amount of power with the grid, P and Q. The reference current vectors to deliver the P and Q powers to the grid are given by:

$$i_p^* = \frac{P}{|v^2|}\, v \tag{54}$$

$$i_q^* = \frac{Q}{|v^2|}\, v_\perp \tag{55}$$

where i_p^* is the active component of the reference current vector and i_q^* is the reactive one. Therefore, the final reference current can be calculated by just adding (54) and (55), as

$$i^* = i_p^* + i_q^* \tag{56}$$

Under balanced sinusoidal conditions, the resulting current references from equation (56) are perfectly sinusoidal, since the module of the voltage, $|v|$, and g and b are constants. However, v and $v_\perp$ are formed by positive- and negative-sequence voltage components when unbalanced grid faults occur. Under such operating conditions, the module $|v|^2$ has oscillations at twice the fundamental grid frequency, i.e..

$$|v^2| = |v^+|^2 + |v^-|^2 + 2|v^+||v^-|\cos(2\omega t + \phi^+ - \phi^-) \tag{57}$$

When the expression of (57) is processed in the denominator of equations (54) and (55), the resulting reference currents i_p^* and i_q^* are not sinusoidal, but consist of high-order harmonics, giving rise to distorted reference signals for the currents to be injected in the phases of the AC-grid. This issue is a serious drawback of the IARC strategy due to the fact that injecting distorted currents requires the implementation of more complex control system.

3.5.2 Positive- and Negative-Sequence Control (PNSC)

The positive and negative-sequence control (PNSC) strategy deals with the calculation of a reference current vector, containing a proper set of positive and negative-sequence components, that is able to cancel out oscillations in the instantaneous powers injected into the grid. The current reference provided with this technique takes as a requirement that the resulting currents to be injected into the grid consist of positive- and negative-sequence components at the fundamental frequency, given as

$$i^* = i^{*+} + i^{*-} \tag{58}$$

where i^{*+} and i^{*-} represent such positive- and negative-sequence components respectively. To determine the expressions for the reference currents generated by the PNSC strategy it is initially assumed that only active power is delivered to the grid. Moreover, it is imposed as a condition that the delivered active power is free of oscillations. Considering these constraints, the reference for active and reactive currents vector are given by

$$i_p^* = g(v^+ - v^-) \; ; \qquad g = \frac{P}{|v^+|^2 - |v^-|^2} \tag{59}$$

$$i_q^* = b(v_\perp{}^+ - v_\perp{}^-) \; ; \qquad b = \frac{Q}{|v^+|^2 - |v^-|^2} \tag{60}$$

In order to study the performance of the instantaneous powers delivered using the PNSC strategy, the positive- and negative-sequence currents injected into the grid are written as the addition of their active and reactive component as follows

$$i^+ = i_p^+ + i_q^+ \tag{61}$$

$$i^- = i_p^- + i_q^- \tag{62}$$

Considering that the current controller used in the power converter guarantees the injection into the grid of the reference currents set by equations (59) and (60) with no error, the following expressions can be written for the instantaneous active and reactive powers delivered by the power converter:

$$p = \underbrace{v^+.i_p^+ + v^-.i_p^-}_{P} + \underbrace{v^+.i_q^+ + v^-.i_q^-}_{0} + \underbrace{v^+.i_p^- + v^-.i_p^+}_{0} + \underbrace{v^+.i_q^- + v^-.i_q^+}_{\tilde{p}} \quad (63)$$

$$q = \underbrace{v_\perp^+.i_q^+ + v_\perp^-.i_q^-}_{Q} + \underbrace{v_\perp^+.i_p^+ + v_\perp^-.i_p^-}_{0} + \underbrace{v_\perp^+.i_q^- + v_\perp^-.i_q^+}_{0} + \underbrace{v_\perp^+.i_p^- + v_\perp^-.i_p^+}_{\tilde{q}} \quad (64)$$

The instantaneous active and reactive power delivered to the grid by applying the PNSC strategy, p and q, differ from the ones provided as a reference, P and Q, by the oscillatory power terms $\tilde{p}$ and $\tilde{q}$. This is due to the interaction between in-quadrature voltage and currents with different sequences. When one of the power references is null, either P or Q, the performance of the instantaneous power when using the PNSC is slightly different. For instance, if just the injection of active power into the network is considered under unbalanced conditions, while the reactive power set-point is equal to zero, the active power oscillations are cancelled. This is due to the fact that the remaining oscillating component in the active power, $\tilde{p}$, depends upon the reactive current components i_q^{*+} and i_q^{*-}. Hence, if the reactive current i_q^* is cancelled, the oscillating term, $\tilde{p}$, does not appear. The same phenomenon occurs with the reactive power oscillations when the active power set-point is set to zero.

3.5.3 Average Active–Reactive Control (AARC)

The average active–reactive control (AARC) strategy calculates the average value of the instantaneous conductance and susceptance, throughout one grid period, and then determines the reference for the active and reactive current vectors i_p^* and i_q^*, operating as:

$$i_p^* = G\, v \quad ; \quad G = \frac{P}{|V_\Sigma^2|} \quad (65)$$

$$i_q^* = B\, v \quad ; \quad B = \frac{Q}{|V_\Sigma^2|} \quad (66)$$

where V_Σ is the collective rms value of the grid voltage, which is defined as:

$$V_\Sigma = \sqrt{\frac{1}{T}\int_0^T |v|^2} = \sqrt{|v^+|^2 + |v^-|^2} \quad (67)$$

Since G and B are constants in the AARC strategy, the voltage and the current waveforms are monotonously proportional. For a given grid voltage$v$, the current references calculated by equations (65) and (66) lead to the smallest possible collective rms value of such currents, I_{Σ}, delivering a constant active power P over one grid period [51]. The lower value of I_{Σ}, the lower are the conduction losses in the system and the higher the efficiency. An analogous conclusion can be reached for the reactive current case.

The same particular cases analyzed for the PNSC can be discussed here. If just reactive power is injected into the grid by using the AARC, the residual instantaneous active power delivered to the network will be equal to zero. Likewise, if only active power is delivered, the residual instantaneous reactive power will be equal to zero.

3.5.4 Balanced Positive-Sequence Control (BPSC)

Considering the same principle used in the AARC strategy, it is possible to find other ways for modifying the value of the conductance and susceptance in the expressions used to calculate the reference currents in order to achieve other objectives. In the case of the balanced positive sequence control (BPSC) strategy, the goal is to inject into the grid a set of balanced sinusoidal currents with only positive-sequence components. This method can be useful if the quality of the currents injected becomes a preferential issue. Moreover, the balanced currents generated by the BPSC strategy can be injected by using simple synchronous controllers, provided that the synchronization system is able to estimate accurately the phase angle of the positive-sequence component of the grid voltage.

The BPSC strategy calculates the active and reactive reference currents as

$$i_p^* = G^+ v^+ \quad ; \quad G^+ = \frac{P}{|v^+|^2} \tag{68}$$

$$i_q^* = B^+ {v_\perp}^+ \quad ; \quad B^+ = \frac{Q}{|v^+|^2} \tag{69}$$

The current vectors of equations (68) and (69) consist of a set of perfectly balanced positive sequence sinusoidal waveforms. Under unbalanced operating conditions, the instantaneous active and reactive power delivered to the grid will differ from P and Q because of the interaction between the positive-sequence injected current and the negative-sequence grid voltage, for example,

$$p = v \,.\, i_p^* = \underbrace{v^+ .\, i_p^*}_{P} + \underbrace{v^- .\, i_p^*}_{\tilde{p}} \tag{50}$$

$$q = v_\perp \,.\, i_p^* = \underbrace{{v_\perp}^+ .\, i_p^*}_{Q} + \underbrace{{v_\perp}^- .\, i_p^*}_{\tilde{q}} \tag{51}$$

where $\tilde{p}$ and $\tilde{q}$ are power oscillations at twice the fundamental utility frequency.

In the BPSC, both the instantaneous active and reactive powers will be affected by oscillations under unbalanced grid conditions. The null value of either the P or Q set-point does not give rise to the cancellation of any power oscillation, which is a difference from previous strategies. On the other hand, this method is the only one that permits not only sinusoidal but also balanced currents to be obtained.

4 Case Study

The case study with simulation results is performed to compare four different strategies to control power oscillations, in terms of improving grid quality, increasing reliability, and performance of the three-phase PV system. The control strategy is based on αβ stationary reference frame with DC-link voltage control based on v_{dc}^2 strategy. The boost converter is used to regulate the PV array voltage with MPPT based on conductance incremental algorithm. The reference currents for the control is generated by four different strategies that aim in controlling power oscillations. The PMR controller is adopted tuned in each frequency that composes the inverter reference current. The inverter current limitation strategies are used to ensure that the inverter operates below its current. The grid voltage sag will be discussed better in next section.

Details about the system parameters and control gains are showed in Table 3 and Table 4. The control loops design are performed considering pole-allocation technique, defining the velocity of the inner loop controllers ten times slower than the effective switching frequency and the outer loop controllers ten times slower than the inner loop controllers. All simulations were implemented in PLECS® environment.

Table 3 - Simulation parameters.

Variable	**Description**	**Value**
f_{sw}	Switching frequency (kHz)	12
V_{grid}	Grid voltage (V)	380
f_n	Grid frequency (Hz)	60
S_n	Rated Power (kVA)	20
V_{cc}	DC bus Voltage (V)	650
C_{bus}	DC bus capacitance (mF)	10
C_f	LCL filter capacitance (μf)	6.33
L_f, L_g	LCL filter inductances (mH)	1
R_1	LCL filter resistance (Ω)	0.0188

Table 4 – Control loops gains.

Parameter	Value
Proportional gain of DC bus voltage loop	0.3770
Integral Gain of dc bus voltage loop	3.9478
Propportional Gain of PMR	7.4164
Integral Gain of PMR	2000

4.1 Voltage Sag Profile

The unbalanced voltage sag is given as Figure 16. There is a decrease on the magnitude in one of the phases of the system, it happens at t = 0.8s, and the magnitude reduces to 20% of the initial value. The system returns to its initial balanced conditions at t = 1.4s. This voltage profile is used as the grid input in the system during all the simulations. It is important to highlight that the disturbance is deep and unsymmetrical, which is very common disturbance in the power grid [7].

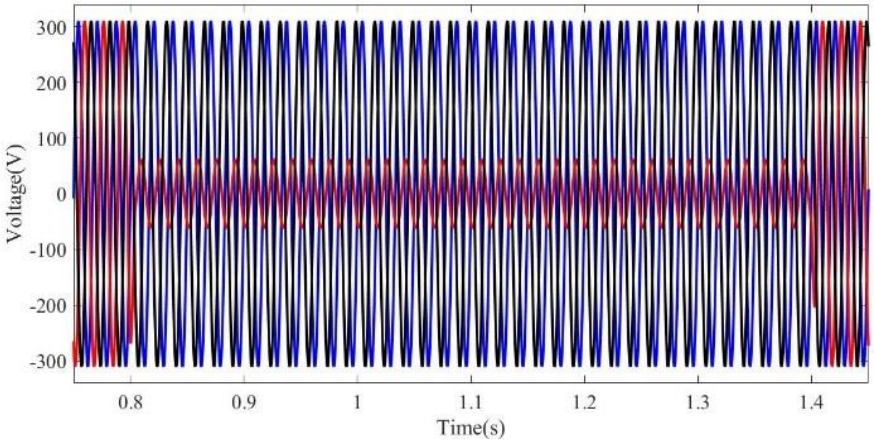

Figure 16 - Unbalanced voltage sag in the grid

4.2 Simulation Results

The focus of this simulation is to compare the four different methods to generate current references when the PV inverter is operating under unbalanced voltage grid conditions. The simulation was repeated four times, with different results for dynamic response and thermal behavior for each one of them.

4.2.1 Dynamic Response

The currents injected into the grid for all four strategies are shown in Figure 17. The IARC method, Figure 17(a), generates a set of unbalanced currents vector, with presence of high orders harmonics. This harmonics are undesirable in the system, and require the presence of more PMR controllers for controlling the current. The second and third strategy generate sets of currents with sinusoidal shapes, but they are not balanced, as it is shown for PNSC method in Figure 17(b), and AARC method in Figure 17(c). The only set of currents totally balanced and sinusoidal, Figure 17(d), is seen on the BPSC method.

Both active and reactive power delivered from the system are presented in Figure 18. IARC method generates active and reactive powers without oscillations during the voltage disturbance. For PNSC method, there is 120 Hz oscillations in the injected reactive power, while there is no observed oscillations in the active power. The opposite happens in the AARC method, no oscillations in reactive power and 120 Hz oscillations in active power, as it was proven in chapter 3. Finally, for the BPSC method, since no negative-sequence components are injected into the grid, oscillations in both active and reactive power occur. In this case, the magnitude of these oscillations is half the magnitude of the other methods, while injecting the same average active and reactive power set-points.

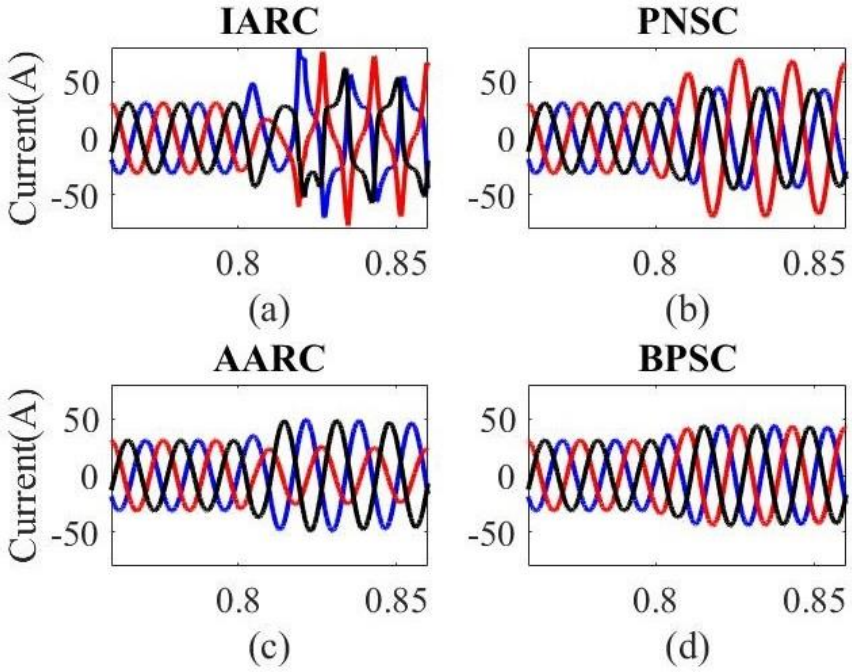

Figure 17 - Currents i_{abc} injected to the grid for the (a) IARC, (b) PNSC, (c) AARC and (d) BPSC methods.

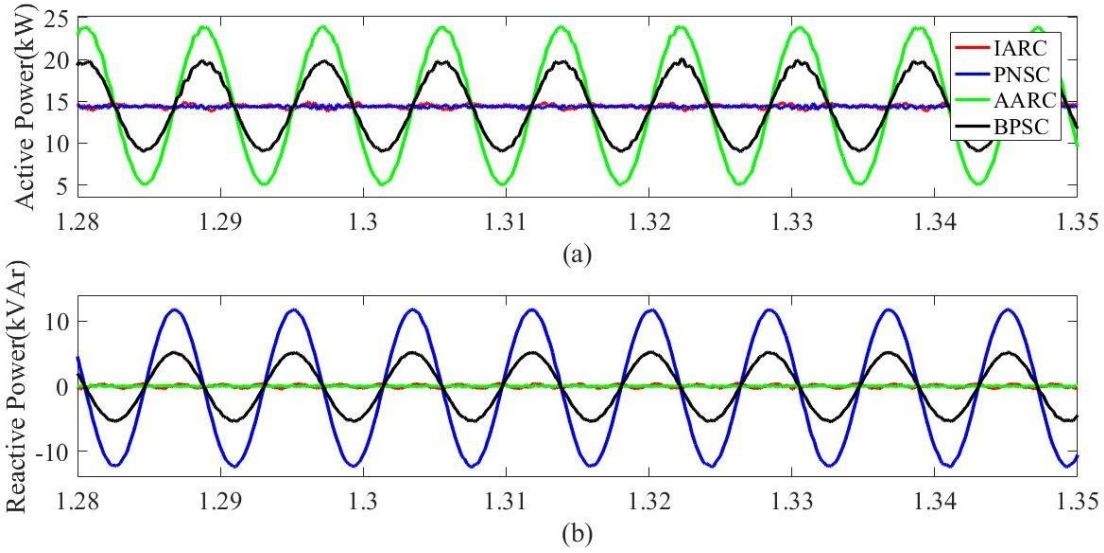

Figure 18 - Reactive power (a) and active power (b) injected to the grid for the different strategies.

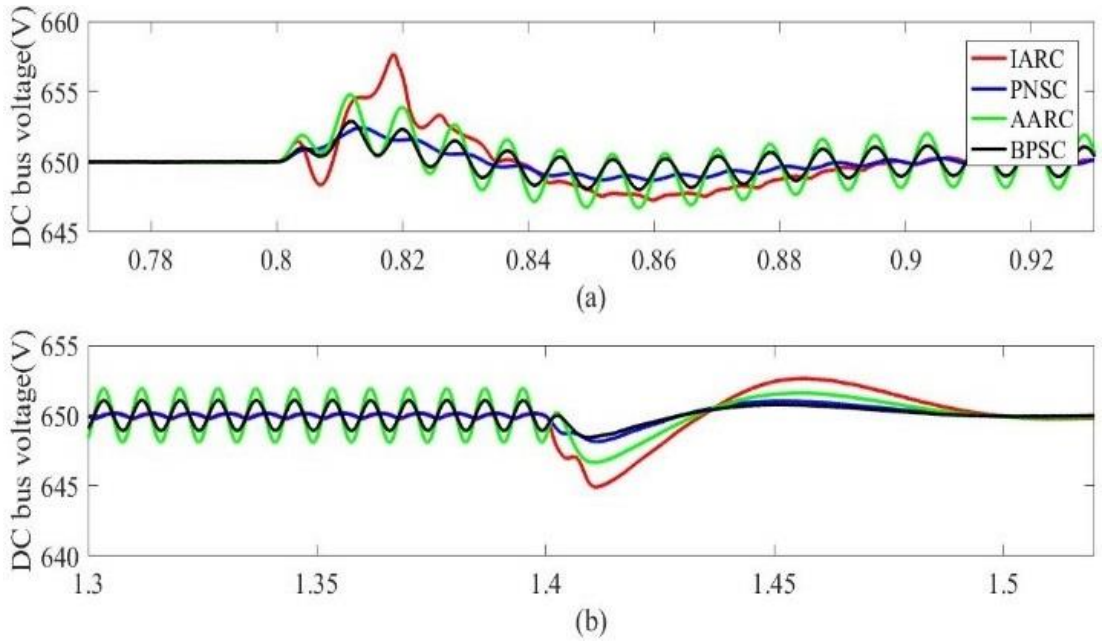

Figure 19 - DC bus voltage for the different strategies, (a) at the start and (b) at the end of the voltage sag.

The last point to take note about the dynamic response of the PV inverter is the DC bus voltage, which is shown in Figure 19. Note that IARC and PNSC methods do not present DC bus voltage oscillations during the voltage sag (after the system stabilizes), while the BPSC presents oscillations with half magnitude of the AARC method. This happens because the DC bus voltage is directly related to the active power injected by the system. In other words, the strategies with less oscillations on active power present less oscillations on the DC bus voltage.

4.2.2 Thermal Behavior and Losses

The thermal behavior of the IGBTs and diode are shown in Figure 20 and 21, respectively. The first row of graphics in each figure shows the temperature oscillations before the disturbance, where the voltages are balanced. In this case, there is no difference between the four methods before the voltage sag. However, the second row in Figure 20 and 21 shows the same IGBT and diode's temperatures during the voltage sag. In all cases, the average temperature increases, which means that there is more thermal stress over the switches when the system is not balanced. The IARC response is not predictable due to the high order frequency harmonics in the current. PNSC method response shows greater thermal stress in one of the phases, which would be harmful to the PV inverter security. The opposite happens in the AARC strategy. Finally, BPSC method shows better thermal response than the other methods.

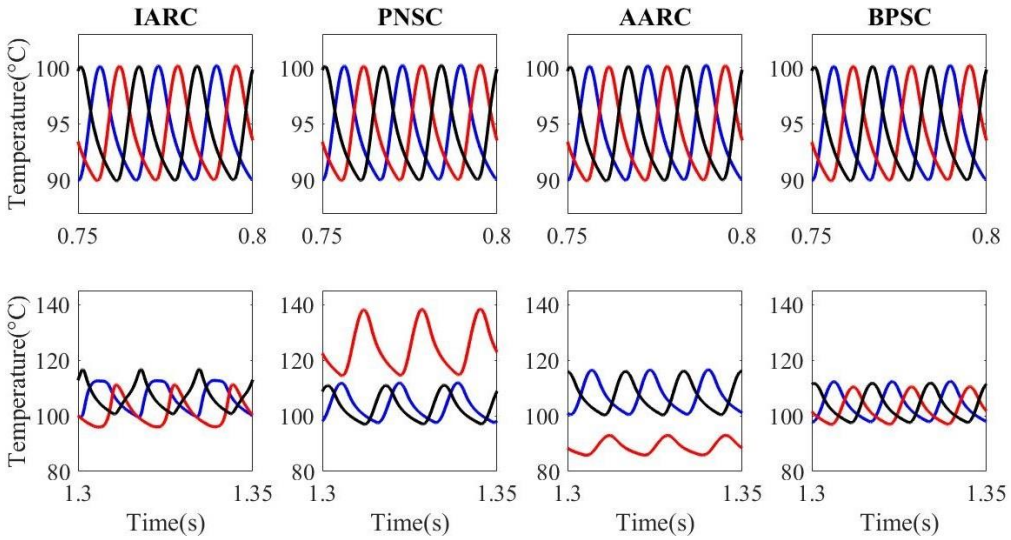

Figure 20 - IGBT's temperature before and during the voltage sag.

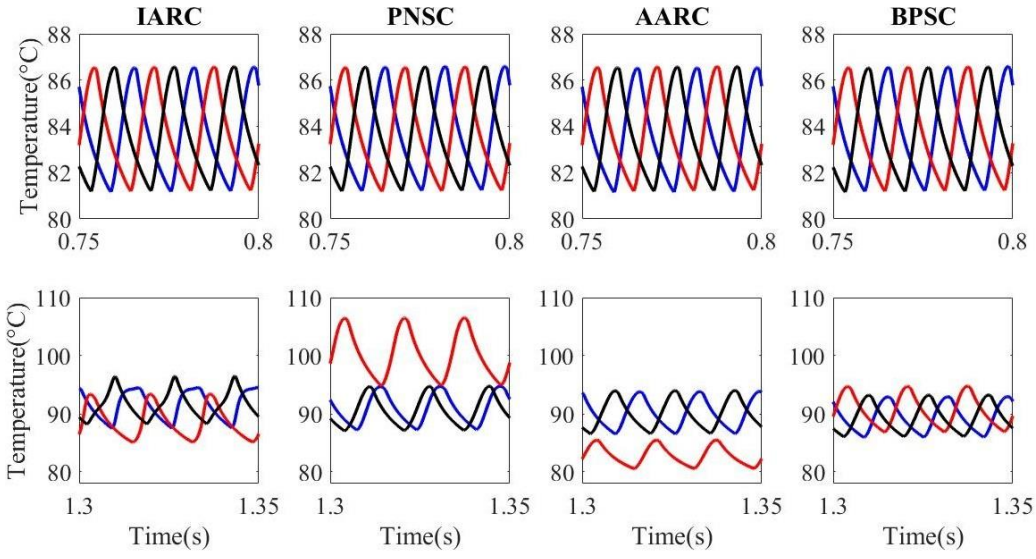

Figure 21 - Diode's temperature before and during the voltage sag.

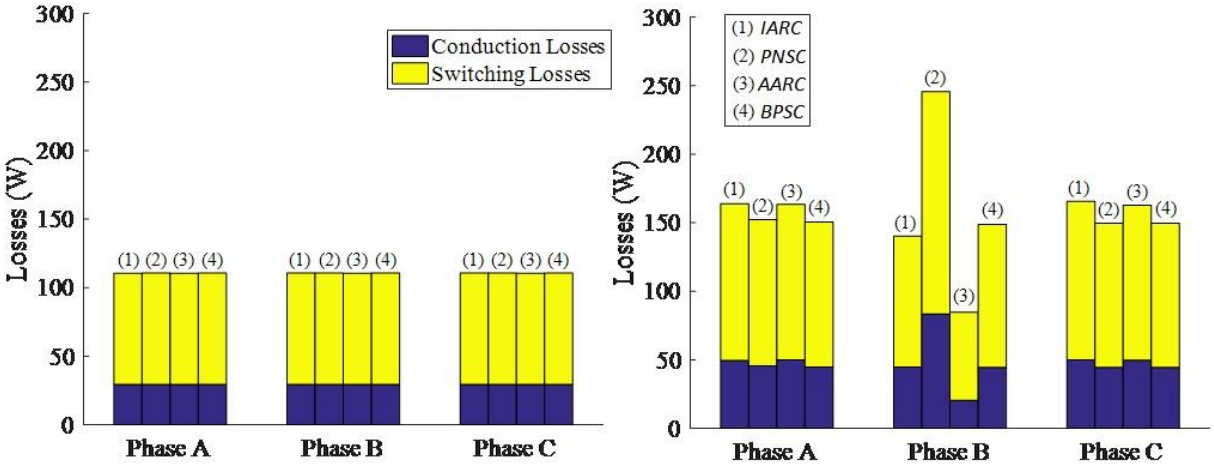

Figure 22 - Conduction and switching losses in each phase before (a) and during (b) the voltage sag.

Finally, the conduction and switching losses are presented in Figure 22. The numbers (1) to (4) represent the methods IARC, PNSC, AARC and BPSC respectively. Figure 22(a) shows the losses before the voltage sag, where the grid voltage is totally balanced. These losses are the same for each phase for all the methods. Figure 22(b) shows the same losses during the unbalanced voltage sag. It is clear to point that, for the PNSC and AARC methods, the switching and conduction losses on the IGBTs and diodes are different for each phase, what could lead to failure in one of the phases before the others. On the other hand, the IARC and BPSC strategies keep balanced the switching and conduction losses. These strategies presented better thermal response, however both possess drawbacks such as high order harmonics and oscillations on active and reactive power delivered.

5 *Conclusion*

This work compare four different strategies for power controlling on a three-phase photovoltaic inverter during a voltage sag on the grid. Each one of these strategies possesses specific characteristics, such as oscillation cancelation on reactive or active power, generation of a set of completely balanced and sinusoidal currents, etc. In addition, this paper explores the system's thermal behavior for each one of the strategies, highlighting the conduction and switching losses during the sag.

Table 5 shows a comparison of the methods, in different aspects. For example, the methods IARC and PNSC present a cancellation of oscillations of active power, which facilitates the control of the DC bus voltage. In other hand, the IARC method injects high order harmonics in the grid, and the PNSC method causes a higher thermal stress in one of the phases, which could make the system less secure and reduce its lifetime. The signs "+" and "-" on the table are used to indicate the system's performance for the different aspects compared in this paper. Where the signs '+' represent a good performance and '-' means that the overall response in this aspect is not good. The PNSC method showed better performance for PV inverter applications. In fact, the lack of oscillations on active power injected to the grid cause the system to have better DC bus voltage control. A stable DC voltage in the system is preferable. However, the PNSC presents worse thermal response compared to the other strategies.

Table 5 - Comparison of power control methods.

	IARC	***PNSC***	***AARC***	***BPSC***
Cancellation of oscillations in the active power	+	+	-	-
Cancellation of oscillations in the reactive power	+	-	+	-
Balanced current injection	-	-	-	+
Absence of high order harmonics	-	+	+	+
Thermal stress and losses	+	-	+	+
Thermal balance	+	-	-	+

5.1 Future Work

Future studies for these power control strategies may include:

- a comparison between the strategies when the injection of reactive power to the grid is also required;
- to propose a dynamic saturation structure for active and reactive power references and currents;
- and lifetime estimation for the switches according to the thermal analysis and losses.

Bibliography

[1] Kristin Seyboth *et al.*, *Renewables 2016 Global Status Report*. 2016.

[2] F. Yang, Q. Sun, Q. Han, and Z. Wu, "for Distributed Photovoltaic Power Generation Systems," vol. 4, no. 2, pp. 414–420, 2016.

[3] E. P. I. Association and E. P. I. A. Epia, "Global Market Outlook for Photovoltaics 2013-2017," *Europe*, no. Mai, p. 74, 2013.

[4] M. G. Simoes *et al.*, "A comparison of smart grid technologies and progresses in Europe and the U.S.," *IEEE Trans. Ind. Appl.*, vol. 48, no. 4, pp. 1154–1162, 2012.

[5] J. Guerrero *et al.*, "Distributed generation: Toward a new energy paradigm," *IEEE Ind. Electron. Mag.*, vol. 4, no. 1, pp. 52–64, 2010.

[6] P. Chiradeja and R. Ramakumar, "An approach to quantify the technical benefits of distributed generation," *IEEE Trans. Energy Convers.*, vol. 19, no. 4, pp. 764–773, 2004.

[7] M. H. J. Bollen, *Understanding Power Quality Problems – Voltage Sags and Interruptions*. New York, USA, 1999.

[8] P. R. Engineering and J. June, "Voltage sags : effects , mitigation and prediction," no. June, pp. 129–135, 1996.

[9] T. R. Kempner, A. Q. Santos, and M. Oleskovicz, "Optimized Monitoring of Voltage Sags in Distribution Systems caused by Balanced and Unbalanced Short-Circuits," pp. 1–5, 2014.

[10] S. Electric and C. Monitor, "Electrical Distribution Solutions Solutions to voltage sags and interruptions," no. figure 2.

[11] R. Teodorescu, M. Liserre, and P. Rodriguez, *Control of Grid Converters under Grid Faults*. 2011.

[12] D. M. Vilathgamuwa, S. Member, and P. C. Loh, "Protection of Microgrids During Utility Voltage Sags," vol. 53, no. 5, pp. 1427–1436, 2006.

[13] S. M. Sreechithra, M. Ieee, P. Jirutitijaroen, S. M. Ieee, and A. K. Rathore, "Impacts of Reactive Power Injections on Thermal Performances of PV Inverters," pp. 7175–7180, 2013.

[14] H. Huang and P. A. Mawby, "A Lifetime Estimation Technique for Voltage Source Inverters," vol. 28, no. 8, pp. 4113–4119, 2013.

[15] H. J. M ¨ oller, "Semiconductors for Solar Cells," *Norwood, MA: Artech House*, 1993.

[16] H. E. Metalsemiconductor, "Solar Cell Contact Resistance-A Review," no. 5, 1984.

[17] D. Sera, R. Teodorescu, and P. Rodriguez, "PV panel model based on datasheet values," no. 4, pp. 2392–2396, 2007.

[18] M. G. Villalva, J. R. Gazoli, and E. R. Filho, "Comprehensive Approach to Modeling and Simulation of Photovoltaic Arrays," vol. 24, no. 5, pp. 1198–1208, 2009.

[19] N. P. Sources and I. Introduction, "PSIM Circuit-Oriented Simulator Model for the Nonlinear Photovoltaic Sources," vol. 42, no. 2, pp. 735–740, 2006.

[20] Y. Kuo, T. Liang, and J. Chen, "Novel Maximum-Power-Point-Tracking Controller for Photovoltaic Energy Conversion System," vol. 48, no. 3, pp. 594–601, 2001.

[21] D. Dondi, D. Brunelli, L. Benini, P. Pavan, A. Bertacchini, and L. Larcher, "Photovoltaic Cell Modeling for Solar Energy Powered Sensor Networks."

[22] F. Wang, J. L. Duarte, and M. A. M. Hendrix, "Active power control strategies for inverter-based distributed power generation adapted to grid-fault ride-through

requirements," *Power Electron. Appl. 2009. EPE '09. 13th Eur. Conf.*, pp. 1–10, 2009.
[23] andW. A. B. W.DeSoto, S.A.Klein, "Improvement and validation of a model for photovoltaic array performance," *Sol. Energy*, vol. 80, no. no.1, pp. 78–88, 2006.
[24] A. Driesse and S. Harrison, "Evaluating the Effectiveness of Maximum Power Point Tracking Methods in Photovoltaic Power Systems using Array Performance Models," pp. 145–151, 2007.
[25] Z. Ozkan, "Three-Phase Inverter Topologies for Grid-Connected Photovoltaic Systems," pp. 498–505, 2014.
[26] H. Xin, Z. Qu, J. Seuss, and A. Maknouninejad, "A self-organizing strategy for power flow control of photovoltaic generators in a distribution network," *IEEE Trans. Power Syst.*, vol. 26, no. 3, pp. 1462–1473, 2011.
[27] M. Liserre, F. Blaabjerg, and S. Hansen, "Design and control of an LCL-filter-based three-phase active rectifier," *IEEE Trans. Ind. Appl.*, vol. 41, no. 5, pp. 1281–1291, 2005.
[28] S. Calligaro, F. Pasut, R. Petrella, and A. Pevere, "Modulation Techniques for Three-Phase Three-Level NPC Inverters : a Review and a Novel Solution for Switching Losses Reduction and Optimal Neutral-Point Balancing in Photovoltaic Applications," pp. 2997–3004, 2013.
[29] C. Charumit and V. Kinnares, "Discontinuous SVPWM Techniques of Three-Leg VSI-Fed Balanced Two-Phase Loads for Reduced Switching Losses and Current Ripple," vol. 30, no. 4, pp. 2191–2204, 2015.
[30] J. Lee, S. Member, K. Lee, S. Member, and F. Blaabjerg, "Open-Switch Fault Detection Method of a Back-to-Back Converter Using NPC Topology for Wind Turbine Systems," vol. 51, no. 1, pp. 325–335, 2015.
[31] M. Aly and M. Shoyama, "Algorithm with Reduced Switching Losses for Three," pp. 330–335, 2014.
[32] M. Mirazimi, "Space Vector PWM Method for Two-Phase Three- Leg Inverters," no. Pedstc, pp. 16–18, 2016.
[33] S. Golestan, S. Member, and J. M. Guerrero, "Transactions on Power Electronics Three-Phase PLLs : A Review of Recent Advances," vol. 8993, no. 1, 2016.
[34] H. Wang and M. Liserre, "Toward Reliable Power Electronics," no. june, pp. 17–26, 2013.
[35] Y. Firouz, M. T. Bina, and B. Eskandari, "Efficiency of three-level neutral-point clamped converters : analysis and experimental validation of power losses , thermal modelling and lifetime prediction," no. December 2012, pp. 209–219, 2013.
[36] and T. R. A. Wintrich, U. Nicolai, W. Tursky, "Application manual power semiconductors," *ISLE-Verlag*. 2011.
[37] Y. Yang, H. Wang, F. Blaabjerg, K. Ma, and D.-A. East, "Mission Profile based Multi-Disciplinary Analysis of Power Modules in Single-Phase Transformerless Photovoltaic Inverters Keywords Mission Profile based Multi-Disciplinary Analysis Method."
[38] R. U. L. Ride-through, K. Ma, and F. Blaabjerg, "Modulation Methods for Neutral-Point-Clamped Wind Power Converter Achieving Loss and Thermal," vol. 61, no. 2, pp. 835–845, 2014.
[39] K. H. Hussein and M. Osakada, "Maximum photovoltaic power tracking : an algorithm for rapidly changing atmospheric conditions," pp. 59–64.
[40] D. Sera, T. Kerekes, R. Teodorescu, and F. Blaabjerg, "Improved MPPT method for rapidly changing environmental conditions," *2006 IEEE Int. Symp. Ind. Electron.*, pp. 1420–1425, 2006.
[41] F. Ansari, "CONTROL OF MPPT FOR PHOTOVOLTAIC SYSTEMS USING

ADVANCED ALGORITHM EPP," no. 25, pp. 25–30, 2009.

[42] I. Laird *et al.*, "Comparative Study of Maximum Power Point Tracking Algorithms for Thermoelectric Generators," pp. 1–6, 2008.

[43] M. G. VILLALVA, "Conversor eletrônico de potência trifásico para sistema fotovoltaico conectado à rede elétrica," UNICAMP:Campinas, 2010.

[44] F. Blaabjerg, R. Teodorescu, M. Liserre, and A. V. Timbus, "Overview of control and grid synchronization for distributed power generation systems," *IEEE Trans. Ind. Electron.*, vol. 53, no. 5, pp. 1398–1409, 2006.

[45] A. G. Yepes, S. Member, F. D. Freijedo, Ó. López, and J. Doval-gandoy, "Analysis and Design of Resonant Current Controllers for Voltage-Source Converters by Means of Nyquist Diagrams and Sensitivity Function," *IEEE Trans. Ind. Electron.*, vol. 58, no. 11, pp. 5231–5250, 2011.

[46] N. Bianchi and M. Dai Pre, "Active power filter control using neural network technologies," *IEE Proceedings-Electric Power Appl.*, vol. 150, no. 2, pp. 139–145, 2003.

[47] A. G. Yepes, S. Member, and F. D. Freijedo, "Effects of Discretization Methods on the Performance of Resonant Controllers," *IEEE Trans. Power Electron.*, vol. 25, no. 7, pp. 1692–1712, 2010.

[48] A. Ovalle, S. Member, G. Ramos, S. Bacha, A. Hably, and A. Rumeau, "Decentralized Control of Voltage Source Converters in Microgrids Based on the Application of Instantaneous Power Theory," vol. 62, no. 2, pp. 1152–1162, 2015.

[49] H. Akagi, E. H. Watanabe, and M. Aredes, "The Instantaneous Power Theory," *Instant. Power Theory Appl. to Power Cond.*, pp. 41–107, 2007.

[50] H. Akagi, Y. Kanazawa, and A. Nabae, "Instantaneous Reactive Power Compensators Comprising Switching Devices without Energy Storage Components Ler p," vol. I, no. 3, pp. 625–630, 1984.

[51] M. Depenbrock, S. Member, V. Staudt, and A. Member, "A Theoretical Investigation of Original and Modified Instantaneous Power Theory Applied to Four-Wire Systems," vol. 39, no. 4, pp. 1160–1167, 2003.